



Article

A Four-Step Method for Estimating Suspended Particle Size Based on In Situ Comprehensive Observations in the Pearl River Estuary in China

Zuomin Wang ^{1,2} , Shuibo Hu ¹, Qingquan Li ^{1,*}, Huizeng Liu ¹, Xiaomei Liao ¹ and Guofeng Wu ¹

- ¹ MNR Key Laboratory for Geo-Environmental Monitoring of Great Bay Area & Guangdong Key Laboratory of Urban Informatics & Guangdong–Hong Kong–Macau Joint Laboratory for Smart Cities & Shenzhen Key Laboratory of Spatial Smart Sensing and Services, Shenzhen University, Shenzhen 518060, China; wangzuomin123@gmail.com (Z.W.); hsb514@163.com (S.H.); huizeng.liu@szu.edu.cn (H.L.); lxmguo@163.com (X.L.); guofeng.wu@szu.edu.cn (G.W.)
- ² College of Civil and Transportation Engineering, Shenzhen University, Shenzhen 518060, China
- * Correspondence: liqq@szu.edu.cn

Abstract: The suspended particle size has great impacts on marine biology environments and biogeochemical processes, such as the settling rates of particles and sunlight transmission in marine water. However, the spatial–temporal variations in particle sizes in coastal waters are rarely reported due to the paucity of appropriate observations and the limitations of particle size retrieval methods, especially in areas with complex optical properties. This study proposed a remote sensing-based method for estimating the median particle size D_v^{50} (calculated with a size range of 2.05–297 μm) that correlates D_v^{50} with the inherent optical properties (IOPs) retrieved from in situ remote sensing reflectance above the water’s surface ($R_{rs}(\lambda)$) in the Pearl River estuary (PRE) in China. $R_{rs}(\lambda)$ was resampled to simulate the Multispectral Instrument (MSI) onboard Sentinel-2A/B, and the wavebands in 490, 560, and 705 nm were utilized for the retrieval of the IOPs. The results of this method had a statistical performance of 0.86, 18.52, 21.28%, and -1.85 for the R^2 , RMSE, MAPE, and bias values, respectively, in validation, which indicated that D_v^{50} could be estimated by $R_{rs}(\lambda)$ with the proposed four-step method. Then, the proposed method was applied to Sentinel-2 MSI imagery, and a clear difference in D_v^{50} distribution which was retrieved from a different time could be seen. The proposed method holds great potential for monitoring the suspended particle size of coastal waters.



Citation: Wang, Z.; Hu, S.; Li, Q.; Liu, H.; Liao, X.; Wu, G. A Four-Step Method for Estimating Suspended Particle Size Based on In Situ Comprehensive Observations in the Pearl River Estuary in China. *Remote Sens.* **2021**, *13*, 5172. <https://doi.org/10.3390/rs13245172>

Academic Editor: Emmanuel Devred

Received: 18 October 2021

Accepted: 17 December 2021

Published: 20 December 2021

Keywords: median particle size; particle size distribution; inherent optical properties; ocean color remote sensing; Sentinel-2

Publisher’s Note: MDPI stays neutral with regard to jurisdictional claims in published maps and institutional affiliations.



Copyright: © 2021 by the authors. Licensee MDPI, Basel, Switzerland. This article is an open access article distributed under the terms and conditions of the Creative Commons Attribution (CC BY) license (<https://creativecommons.org/licenses/by/4.0/>).

1. Introduction

The suspended particle size in marine water has great impacts on marine biology environments and biogeochemistry processes (e.g., the settling velocity, resuspension, aggregates, and carbon cycle of particles [1]), and it has been proven to have a significant effect on the inherent optical properties (IOPs) of water so as to change the signals of ocean color remote sensing [2]. Hence, it is of great significance to obtain the characteristics of particle size. The median particle size (D_v^{50}) [3–5], which is the diameter corresponding to the 50th percentile of the accumulated volume concentration, is frequently used to describe the particle size distribution (PSD) of marine systems [6]. The parameter D_v^{50} represents the proportional relationship between small particles and large particles in the particle size range; that is to say, a larger value of D_v^{50} indicates that larger particles are more dominant, and vice versa [2,5]. Therefore, the spatiotemporal dynamics of D_v^{50} can describe the characteristics of the particle size in marine water.

To determine the particle size, various particle sizing instruments, including particle imaging systems (FlowCAM) [7], electrical impedance particle sizers (Coulter Counter) [8],

and laser diffractometers (LISST) [9], have been applied in both oceanic and inland water observation. Although many valuable observations have been carried out using these instruments worldwide, the spatial–temporal variations in D_v^{50} have seldom been investigated due to the limitation of traditional observation methods [10]. Ocean color remote sensing provides the possibility of monitoring the state of the ocean routinely and in a cost-effective manner at a large scale [11], which makes it possible to observe D_v^{50} more appropriately.

According to Mie theory [12], the particle size and particle composition make significant contributions to the scattering properties of particle assemblages that are suspended in marine water, and thus, some studies have suggested a relationship between scattering or backscattering and the particle size. Bowers et al. (2007) [3] developed an algorithm for particle size estimation by building a relationship with light scattering per unit concentration, and van der Lee et al. (2009) [4] applied this method to a much larger set of MODIS imagery to obtain the monthly average particle size in the southern Irish Sea. Qing et al. (2014) [13] utilized the ratio of green to red channels to build the empirical model for particle size estimation in the Bohai Sea in China. Sun et al. (2016) [5] evaluated the inadequacies of the above studies and proposed a hybrid method by combining analytical, semi-analytical, and empirical processes to estimate D_v^{50} from remote sensing reflectance ($R_{rs}(\lambda)$). These studies indicate that PSD can be estimated by a remote sensing method.

Ocean color satellite sensors such as SeaWiFS, MODIS, MERIS, and OLCI were designed specifically to observe the water's bio-optical properties. However, the mixed pixel problems caused by low spatial resolutions of their imagery sometimes limit their application when observing coastal waters or areas close to islands, particularly in areas with high variability of suspended particles [14]. The multi-spectral instrument (MSI) sensor onboard the Sentinel-2 A/B satellite can obtain higher spatial resolution imagery (10 m at visible and near infrared bands), with a relatively short revisit interval (10 days for one satellite and 5 days for double satellites) compared with other sensors with high spatial resolutions, such as Landsat-8. Despite Sentinel-2 being designed for global land monitoring, some studies have demonstrated its potential for assessing coastal and inland water quality [14–16].

The Pearl River estuary (PRE) is a tropical estuary, and the hydrodynamic conditions in the PRE are complex due to many factors, such as river discharges, topography, tides, and monsoons [17]. It is heavily influenced by frequent anthropogenic activities, such as industrialization and urbanization. The suspended sediment concentration in the coastal water and its variation as impacted by anthropogenic activity have been analyzed by many studies. However, the spatial–temporal variation of the suspended particle size in this area has rarely been reported. This study aimed to develop a method for retrieving the suspended particle size in the water areas with complex optical properties based on ocean color remote sensing and furthermore to apply the proposed method to Sentinel-2 MSI data for obtaining the spatiotemporal variation of the suspended particle size in the PRE. The findings of this study may provide information for understanding the characteristics of the particle size distributions in optically complex coastal waters.

2. Materials and Methods

2.1. Study Area and Fieldwork

The complex hydrodynamics of the study site are determined by many physical factors that were mainly contributed by the Pearl River discharge, coastal current, and oceanic waters from the South China Sea [18]. In this study, a total of three trips were conducted (Figure 1). Two of them were around four islands in the central and western area of the PRE (Neilingding, Dachan, Xiaochan, and Mazhou) in spring (21 May and 22 May) and autumn (20 September) of 2019, and the other trip was to an observation section on 8 January 2020. A total of 39 observations were conducted at 25 sites (N1–N9, S1–S8, and P1–P8), including 39 inherent optical property data (i.e., absorption coefficient, attenuation coefficient

and scattering coefficient), 39 PSD datasets, and only 16 apparent optical property data (i.e., $R_{rs}(\lambda)$) due to bad observation conditions (Table 1).

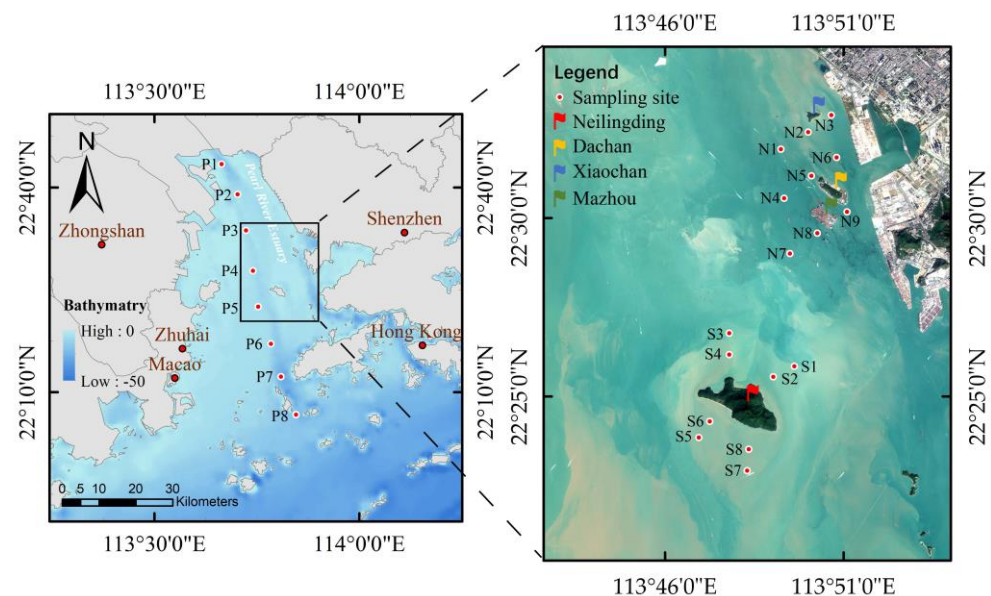


Figure 1. Study area and sampling sites.

Table 1. Observation stations with respect to three trips, including IOP, PSD, and AOP data.

Data Type	2019		2020	Count
	21 May, 22 May	20 September	8 January	
IOPs	N1–N6, S1–S8	N1–N9, S1–S8	P1–P8	39
PSD	N1–N6, S1–S8	N1–N9, S1–S8	P1–P8	39
AOPs	No data	N1–N8, S1–S8	No data	16

2.2. PSD Acquisition

In this study, a LISST-200X Type-C particle size analyzer (Sequoia Scientific, Inc., Bellevue, WA, USA) was used for PSD measurements. It is an upgraded version of the LISST-100X, which is a widely used instrument for in situ PSD measurements in marine waters [19–21]. The LISST-200X type-C has 36 size bins that cover a size range from 1 to 500 μm , and the size spectrum is logarithmically spaced [22]. For each bin, the upper size is 1.18 times the lower, and the width varies from 0.26 to 80 μm , with the exception of bin 1. The LISST uses particle diffraction, which is received by an optics receiving system formed by 36 concentric ring-shaped detectors, to perform a nonintrusive measurement of the volume concentration of suspended particles through a collimated laser beam (670 nm) [23–25].

Before the trip, the LISST was calibrated with Milli-Q water. The particle volume concentration ($V(D)$ in $\mu\text{L/L}$) in the 36 size bins could be derived from the manufacturer-provided software LISST-SOP after in situ measurements. In addition, the total volume concentration ($V_{\text{tot}}(D)$) could be retrieved by a simple summation calculation of $V(D)$ in all the size bins. There were two particle shape models for the $V(D)$ data derived when using the LISST-SOP software, and we selected the irregularly shaped model, as it was more fitting than the spherical model when working with natural waters [22]. As a parameter for characterizing the particle size, the in situ D_v^{50} corresponded to the particle diameter when the cumulated $V(D)$ reached 50% of the $V_{\text{tot}}(D)$, which was calculated by summarizing the $V(D)$ between the 4th and 33rd size bins (i.e., a size range from 2.05 to 297 μm), since the data in the biggest and smallest bins were not stable.

2.3. Optical Property Measurements

In the case of the apparent optical properties (AOPs), the remote sensing reflectance ($R_{rs}(\lambda)$) was measured using an ASD FieldSpec 4 spectroradiometer (Analytical Spectral Devices, Boulder, CO, USA) which covered a spectral range of 350–2500 nm with 1 nm intervals. The measurements were carried out following the NASA marine optical protocol [26]. We adopted the observing geometry of a zenith angle of 40° from the water's surface and an azimuth angle of 135° from the direction of the sun irradiance to perform the measurements, thus avoiding the shadow of the ship and direct irradiance from the sun [27]. Aside from that, the foam patches and whitecaps were kept away from the field of view to avoid signal interference by them. The measured $R_{rs}(\lambda)$ was calculated with Equation (1):

$$R_{rs}(\lambda) = \frac{L_w(\lambda) - \rho L_{sky}(\lambda)}{\pi L_p(\lambda) / \rho_p} \quad (1)$$

where L_w , L_{sky} , and L_p stand for the radiances measured from the water's surface, sky, and a standard gray reference panel, respectively; ρ_p is the diffuse reflectance of the reference panel; and ρ is the dimensionless air–water reflectance, which is always a constant value (here, we adopted 0.025 as the value due to the wind speed being lower than 5 m/s) [28].

As for the IOPs, the absorption coefficient ($a(\lambda)$ in m^{-1}) and attenuation coefficient ($c(\lambda)$ in m^{-1}) were obtained by an AC-S spectral absorption and attenuation meter (WET Labs, USA). As the scattering coefficient of CDOM could be disregarded, the particle scattering ($b_p(\lambda)$ in m^{-1}) was calculated through the relationship $b_p(\lambda) = c(\lambda) - a(\lambda)$ [29]. The AC-S instrument provides 84 channels within the range of about 400–730 nm with approximately 4-nm steps [30]. The backscattering coefficient of the suspended particles ($b_{bp}(\lambda)$ in m^{-1}) was obtained using a BB9 (WET Labs, Philomath, OR, USA) with 9 bands (412, 440, 488, 532, 595, 695, and 715 nm for backscattering and 2 bands for CDOM and Chl-*a* fluorescence). For the postprocessing and correction of AC-S and BB9, the temperature and salinity data were measured synchronously with an SBE37 CTD (Sea-Bird Electronics, Bellevue, WA, USA). Before the trip, the AC-S, BB9, and CTD instruments would be sent to the manufacturer for periodic factory calibrations, and the instruments were rinsed with pure water immediately after each observation. To obtain accurate absorption and attenuation information, temperature and salinity corrections were performed on the raw data by following the ac Meter Protocol Document [30], and the effects of reflective tube scattering were corrected by following the method proposed by Sullivan et al. (2006) [31]. The raw BB9 data were corrected by following the BB9 User's Guide [32].

2.4. Sentinel-2 A/B MSI Image

The level-1C (L1C) Sentinel-2 A/B MSI images were obtained from the European Space Agency's (ESA) Copernicus Open Access Hub. Two cloudless images were selected from both the wet season (22 September 2019) and the dry season (30 January 2020) in this study. Unfortunately, there were no matchups with the sampling sites due to clouds. The L1C images were projected to Universal Transverse Mercator/World Geodetic System 84 (UTM/WGS84) and resampled to a 10-m spatial resolution. To retrieve the $R_{rs}(\lambda)$ above the water's surface, the Case 2 Regional Coast Colour processor (C2RCC) [33], which has been proven to perform well in atmosphere correction over coastal areas [34,35], was applied to carry out atmosphere correction. These processes were completed in the free Sentinel Application Platform (SNAP) version 8.0.0 with the C2RCC plug-in.

2.5. D_v^{50} Retrieval

A four-step method was proposed for D_v^{50} retrieval in this study (Figure 2), and the steps are as follows.

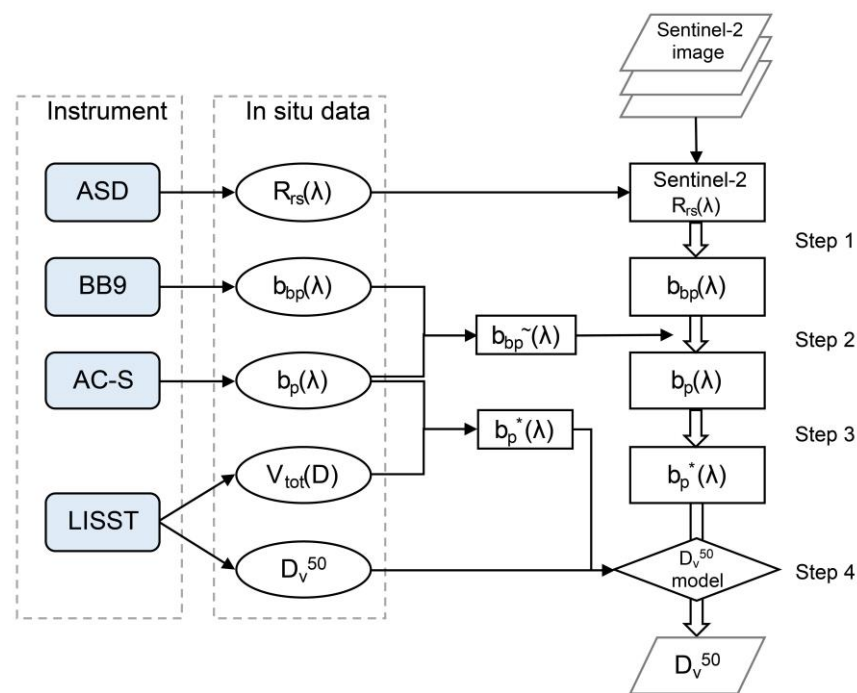


Figure 2. D_v^{50} retrieval schematic flow chart.

2.5.1. Step 1

The in situ $R_{rs}(\lambda)$ was simulated to the Sentinel-2 MSI equivalent $R_{rs}(\lambda)$ with the Sentinel-2 corresponding spectral response function (SRF) (Equation (2)), and the $b_{bp}(\lambda)$ retrieval algorithm was developed using the simulated $R_{rs}(\lambda)$. For $b_{bp}(\lambda)$ retrieval, a quasi-analytical algorithm (QAA) based on radiative transfer theory was applied to invert $R_{rs}(\lambda)$ to the water IOPs [36]. The updated versions (e.g., QAA-v5 and QAA-v6) were developed both for open oceanic and coastal waters [37]. In the QAA, the relationship between $R_{rs}(\lambda)$ and the spectral backscattering and absorption coefficients can be written as the following equations (Equations (3)–(5)):

$$R_{rs(\text{sentinel-2})}(\lambda) = \frac{\int_{\lambda_1}^{\lambda_2} R_{rs}(\lambda) \text{SRF}(\lambda) d(\lambda)}{\int_{\lambda_1}^{\lambda_2} \text{SRF}(\lambda) d(\lambda)} \quad (2)$$

$$r_{rs}(\lambda) = \frac{R_{rs}(\lambda)}{(0.52 + 1.7 \times R_{rs}(\lambda))} \quad (3)$$

$$u(\lambda) = \frac{b_b(\lambda)}{a(\lambda) + b_b(\lambda)} \quad (4)$$

$$r_{rs}(\lambda) = g_0 \times u(\lambda) + g_1 \times u(\lambda)^2 \quad (5)$$

where $R_{rs}(\lambda)$ is the spectral remote sensing reflectance just below the water surface; $a(\lambda)$ and $b_b(\lambda)$ are the total absorption coefficient and total backscattering coefficient, respectively; and $u(\lambda)$ is the ratio of the backscattering coefficient to the sum of the absorption coefficient and backscattering coefficient. The coefficients g_0 (0.0895) and g_1 (0.1247) were proposed for relatively turbid coastal waters through radiative transfer theory [36]. Several studies showed that if the NIR band was used, $a(\lambda)$ could be replaced by the absorption coefficient of pure water $a_w(\lambda)$ due to the absorption of water being much larger than those for other substances [38,39]. We tested the applicability in this study, and our results show that

absorbance above 95% was contributed by pure water. Hence, we took 705 nm of the Sentinel-2 bands as the reference band of $b_{bp}(\lambda)$ (Equation (6)):

$$b_{bp}(705) = \frac{u(705) \times a_w(705)}{1 - u(705)} - b_{bw}(705) \quad (6)$$

where the values of $a_w(705)$ and $b_{bw}(705)$ (backscattering coefficient of pure water) are known [40]. In this study, wavelengths of 490 and 560 nm were used in our empirical model to estimate the slope of particle backscattering coefficient Y (Equation (7)) rather than 443 nm, as it suffered from larger errors in atmospheric correction due to the high absorption of CDOM and suspended particles in a coastal environment. Finally, $b_{bp}(\lambda)$ can be calculated with the estimated $b_{bp}(705)$ and slope Y (Equation (8)):

$$Y = 2.0 \left\{ 1 - 1.2 \exp \left[-0.9 \times \frac{r_{rs}(490)}{r_{rs}(560)} \right] \right\} \quad (7)$$

$$b_{bp}(\lambda) = b_{bp}(705) \times \left(\frac{705}{\lambda} \right)^Y \quad (8)$$

2.5.2. Step 2

The backscattering ratio ($b_{bp}^{\sim}(\lambda)$) was used to obtain $b_p(\lambda)$ (Equation (9)). It should be noted that $b_{bp}^{\sim}(\lambda)$ is usually not a constant value due to some physical properties (such as the component, size, and structure) of the suspended particles [41–43]. However, for some specific study areas, $b_{bp}^{\sim}(\lambda)$ is regarded a constant or to be within certain limits [44,45]. In this study, we performed a least square fitting using in situ measured $b_{bp}(\lambda)$ and $b_p(\lambda)$ to obtain $b_{bp}^{\sim}(\lambda)$ and to evaluate the applicability of $b_{bp}^{\sim}(\lambda)$ as a constant in the present study area:

$$b_p = \frac{b_{bp}}{b_{bp}^{\sim}} \quad (9)$$

2.5.3. Step 3

In general, $b_p(\lambda)$ is affected by the total suspended matter (TSM), the scattering efficiency (Q_{be}), the apparent density (ρ_a), and the mean diameter weighted by the area (D_A), and it is most affected by the TSM. Hence, the mass-specific scattering or backscattering (i.e., $b_p(\lambda)$ or $b_{bp}(\lambda)$ divided by the TSM) are usually used to estimate the particle size [11]. However, as we can see from Equation (10), the mass-specific scattering is affected not only by D_A but also by the value ρ_a multiplied by D_A . The volume-specific scattering coefficient ($b_p^*(\lambda)$), which was calculated by the ratio of $b_p(\lambda)$ to $V_{tot}(D)$, was introduced in this study because the scattering per unit volume concentration was likely to scale with the particle diameter (Equation (11)). To calculate the value of $b_p^*(\lambda)$, $V_{tot}(D)$ should first be estimated according to Equation (11). The $V_{tot}(D)$ prediction model was calibrated by $b_p(\lambda)$ and $b_{bp}(\lambda)$ separately, for $b_p(\lambda)$ and $b_{bp}(\lambda)$ were both considered to be dependent on the suspended particle concentration. The accuracy of the $V_{tot}(D)$ prediction models calibrated by $b_p(\lambda)$ and $b_{bp}(\lambda)$ were compared, and we adopted the one with better performance:

$$b_p = \frac{3}{2} \frac{Q_{be}}{\rho_a D_A} TSM = \frac{3}{2} \frac{Q_{be}}{D_A} V_{tot}(D) \quad (10)$$

$$b_p^* = \frac{b_p}{V_{tot}(D)} = \frac{3}{2} \frac{Q_{be}}{D_A} \quad (11)$$

2.5.4. Step 4

D_v^{50} was obtained from the D_v^{50} model developed using in situ calculated $b_p^*(\lambda)$ and D_v^{50} . In the past few years, several D_v^{50} models have been proposed for certain areas. For instance, an inverse proportion model and a negative power function model were

developed for the Irish Sea and the nearshore waters of Imperial Beach, respectively [3,46]. Then, the negative power function model was optimized and applied in the Bohai Sea and Yellow Sea [5]. All of the above models were developed based on the relationship between D_v^{50} and the mass-specific $b_p(\lambda)$ or $b_{bp}(\lambda)$. We validated the previous models in our study area and proposed a negative exponential function model for D_v^{50} estimation. We compared these models calibrated by $b_p^*(\lambda)$ and $b_{bp}^*(\lambda)$ separately, and we adopted the one with the best performance.

2.6. Accuracy Assessment

To assess the consistency of the estimated in situ measured values, the root mean squared error (RMSE) (Equation (12)), mean absolute percentage error (MAPE) (Equation (13)), and bias (Equation (14)) were used in this study:

$$\text{RMSE} = \sqrt{\frac{1}{N} \sum_{i=1}^N (y'_i - y_i)^2} \quad (12)$$

$$\text{MAPE} = \frac{1}{N} \sum_{i=1}^N \left| \frac{y'_i - y_i}{y_i} \right| \quad (13)$$

$$\text{bias} = \frac{1}{N} \sum_{i=1}^N (y'_i - y_i) \quad (14)$$

where y'_i is the predicted value, y_i is the measured value, and N is the number of samples.

3. Results

3.1. Optical Properties and PSD

A summary of the measured data (including the optical properties and particle size parameters) is shown in Table 2. All of the parameters showed a wide range with a high C.V. value, which indicated the large variation of the optical properties and PSD in the study area. It needs to be mentioned that the wavelength of 532 nm was used both for $b_p(\lambda)$ and $b_{bp}(\lambda)$, because signal saturation appeared in the red and NIR bands for in situ BB9 backscattering measurement (especially at 695 and 715 nm). We also abandoned the blue bands for the reason that large errors would appear when calculating $b_{bp}(\lambda)$ at wavelengths far from the reference wavelength in the NIR region.

Table 2. Descriptive statistics for particulate backscattering $b_{bp}(\lambda)$, scattering $b_p(\lambda)$, volume-specific scattering $b_p^*(\lambda)$, coefficients at 532 nm, total volume concentration $V_{\text{tot}}(D)$, and median particle size D_v^{50} . S.D. = standard deviation; C.V. = coefficient of variation; and N = number of observations.

Variable	Units	Min	Max	Mean	S.D.	C.V. (%)	N
$b_{bp}(532)$	m^{-1}	0.02	0.22	0.11	0.1	44.3	39 *
$b_p(532)$	m^{-1}	1.26	14.34	5.85	2.8	47.2	39
$b_p^*(532)$	m^2/mL	0.04	0.34	0.18	0.1	40.7	39
$V_{\text{tot}}(D)$	$\mu\text{L}/\text{L}$	9.37	144.76	38.77	26.8	69.0	39
D_v^{50}	μm	28.89	263.02	103.10	74.6	72.4	39

* For $b_{bp}(532)$, 37 measurements were available from 39 measurements due to the saturation of the signal that appeared in 2 observations.

3.2. D_v^{50} Model Development

The validation of the QAA for $b_{bp}(532)$ retrieval is shown in Figure 3a. The QAA estimated and in situ measured $b_{bp}(532)$ values showed a good fit ($R^2 = 0.85$, $\text{RMSE} = 0.02$), with $\text{MAPE} = 17.2\%$ and $\text{bias} = -0.0021$. As we can see, the scattered dots were mostly close to the 1:1 line. This finding indicates that the QAA method held good potential for $b_{bp}(\lambda)$ retrieval in our study area. The backscattering ratio $b_{bp}^{\sim}(\lambda)$ was derived from the

least square fitting using the in situ measured $b_{bp}(\lambda)$ and $b_p(\lambda)$, with a high R^2 value of 0.94 and a low RMSE value of 0.012 (Figure 3b). The slope of the fitted equation was 0.0202, which was the ratio of $b_{bp}(\lambda)$ and $b_p(\lambda)$ and was equivalent to $b_{bp}^*(\lambda)$ in this study.

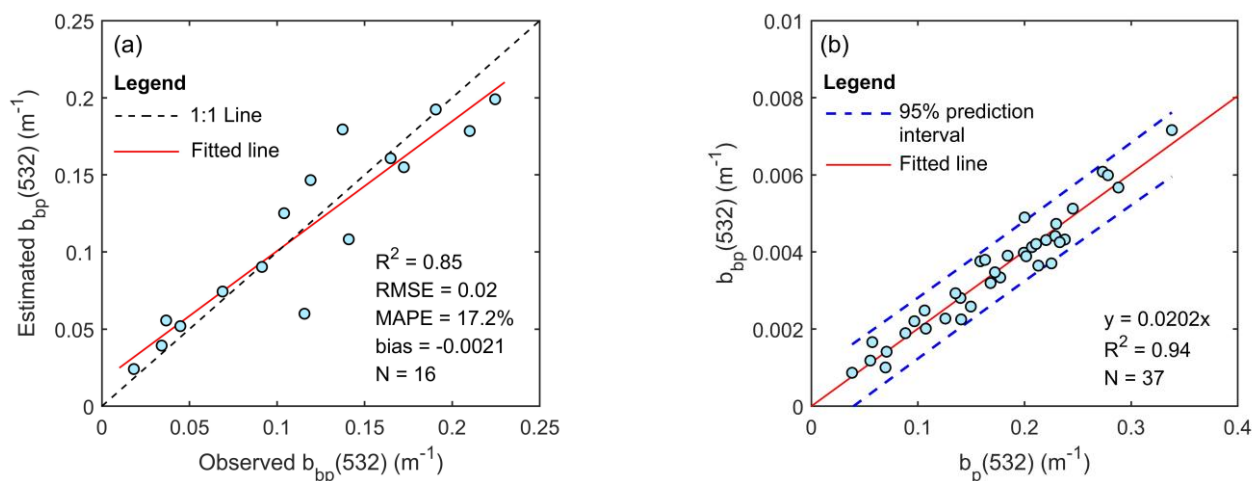


Figure 3. (a) Validation of QAA method for $b_{bp}(532)$ retrieval. (b) The relationship between $b_{bp}(532)$ and $b_p(532)$.

As for $V_{tot}(D)$ retrieval, we compared the results of the empirical models calibrated by $b_p(532)$ and $b_{bp}(532)$. The $V_{tot}(D)$ retrieval model calibrated by $b_p(532)$ held a higher accuracy, with an R^2 of 0.75 (Figure 4a), and the $V_{tot}(D)$ retrieval model calibrated by $b_{bp}(532)$ showed a lower accuracy, with an R^2 of 0.72 (Figure 4b). Moreover, signal saturation appeared in two sites for the $b_{bp}(532)$ data, which indicates that $b_{bp}(532)$ might not be available in high-turbidity water. Hence, $b_p(532)$ was used to calculate $V_{tot}(D)$ in this study.

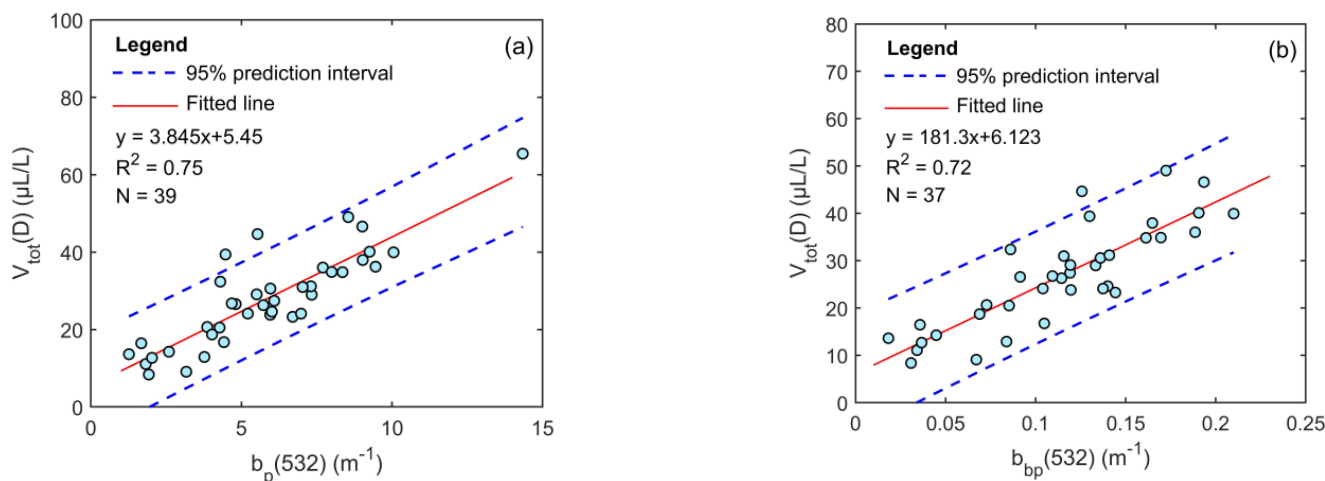


Figure 4. The $V_{tot}(D)$ estimation from (a) $b_p(532)$ and (b) $b_{bp}(532)$.

For D_v^{50} retrieval, 23 simultaneous $b_p^*(\lambda)$, $b_{bp}^*(\lambda)$, and D_v^{50} datasets were used in the calibration of the inverse proportion model (Figure 5a for $b_p^*(\lambda)$ and Figure 5b for $b_{bp}^*(\lambda)$), negative power function model ((Figure 5c for $b_p^*(\lambda)$ and Figure 5d for $b_{bp}^*(\lambda)$)), and negative exponential function model (Figure 5e for $b_p^*(\lambda)$ and Figure 5f for $b_{bp}^*(\lambda)$). The results for all models are shown in Table 3. Overall, a good fit ($R^2 = 0.85$, RMSE = 33.5 μm) was found by the proposed model for the relationship between $b_p^*(\lambda)$ and D_v^{50} (Figure 5e). The proposed model also showed the potential ($R^2 = 0.78$, RMSE = 41.3 μm) in the relationship between $b_{bp}^*(\lambda)$ and D_v^{50} (Figure 5f), while the other two models obtained poorer results

for estimating D_V^{50} . The findings indicated that the negative exponential model performed best in our study area.

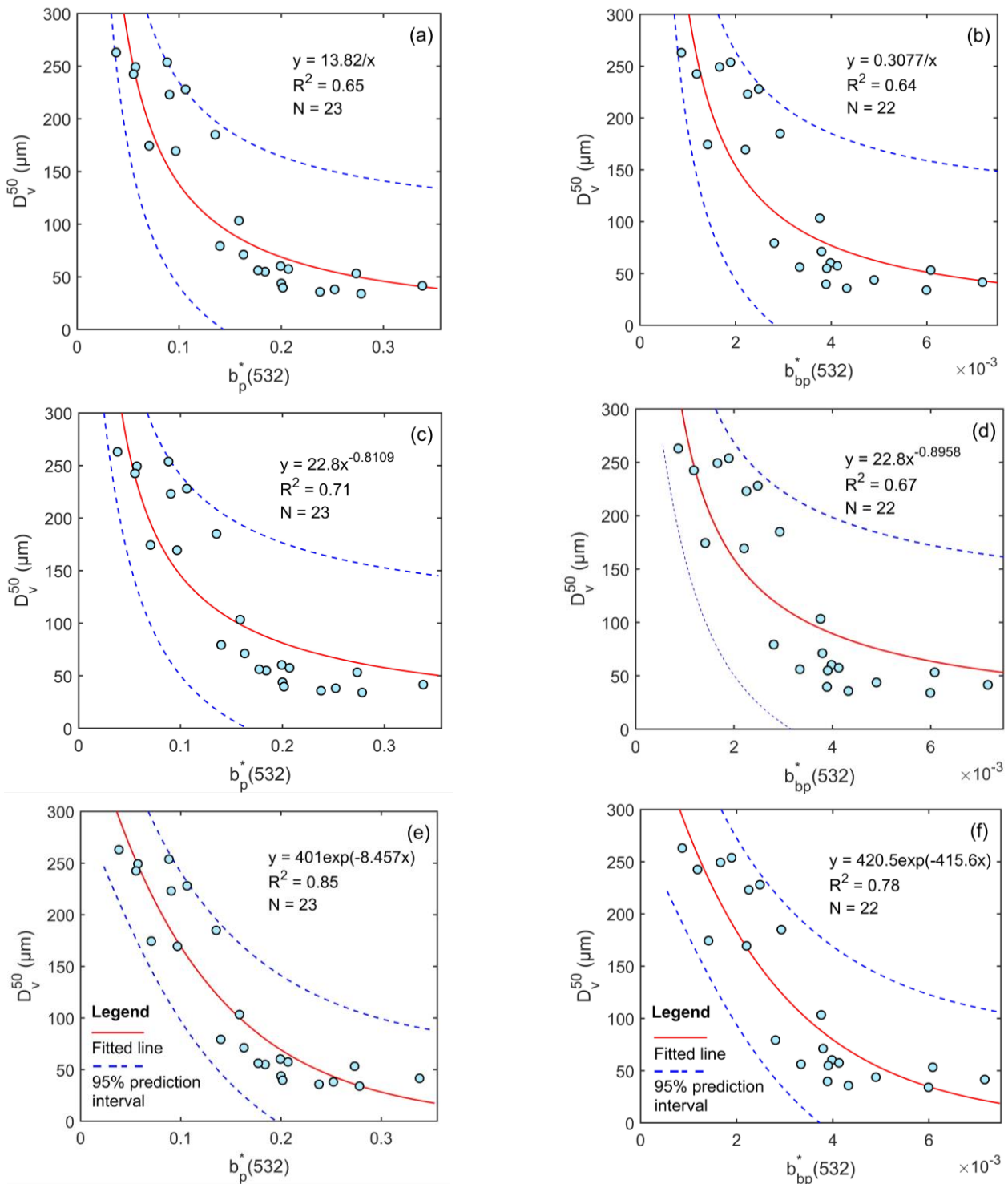


Figure 5. The performance of D_V^{50} retrieval models with $b_p^*(532)$ ((a) inverse proportion, (c) negative power function, and (e) negative exponential function) and $b_{bp}^*(532)$ ((b) inverse proportion, (d) negative power function, and (f) negative exponential function).

Table 3. Comparison of D_v^{50} models reported by previous studies and that proposed in this study in calibration.

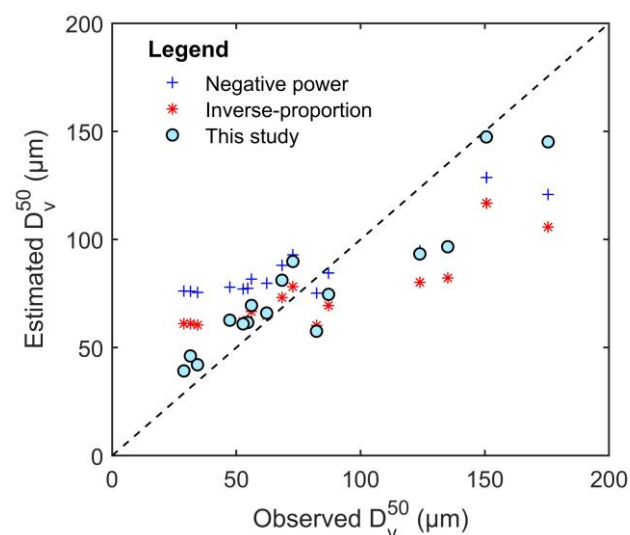
Relation	Model	R^2	RMSE (μm)	Reference
D_v^{50} vs. b_p^*	Inverse proportion	0.65	50.78	Bowers et al. (2007)
	Negative power function	0.71	48.9	Woźniak et al. (2010)
	Negative exponential function	0.85	33.5	This study
D_v^{50} vs. b_{bp}^*	Inverse proportion	0.64	51.6	Bowers et al. (2007)
	Negative power function	0.67	50.7	Woźniak et al. (2010)
	Negative exponential function	0.78	41.3	This study

3.3. D_v^{50} Model Validation and Application

In this study, 16 in situ measurements were used to validate the performance of the D_v^{50} retrieval models proposed by previous studies and developed in this study. The model validation results showed that the proposed method performed well, with an R^2 of 0.86, RMSE of 18.52 μm , MAPE of 21.28%, and bias of -1.85 (Table 4). The scattered dots were mostly close to the 1:1 line, except for some dots with large D_v^{50} values (Figure 6) due to a shortage of training data for model calibration, especially in the case of the large D_v^{50} samples. The findings proved that D_v^{50} could be estimated using the remote sensing method.

Table 4. Performance comparison of D_v^{50} models reported by previous studies and that proposed in this study in validation.

Model	R^2	RMSE	MAPE	Bias
Inverse proportion	0.78	30.28	31.6%	-6.01
Negative power function	0.79	31.17	32.36%	8.74
This study	0.86	18.52	21.28%	-1.85

**Figure 6.** Validation of the D_v^{50} retrieval models proposed by previous studies and developed in this study.

The proposed D_v^{50} model was further applied to the remote-sensed ocean color data. After applying the proposed method to the Sentinel-2 MSI images, we obtained the D_v^{50} distribution at different times in our study area (Figure 7). The satellite-retrieved D_v^{50} values ranged from approximately 50 to 180 μm . It can be seen that there existed obvious differences in the D_v^{50} distribution in both time and space; D_v^{50} on 30 January 2020 was

higher than that on 22 September 2019 in most areas, with the exception of the western area of the PRE, and D_v^{50} in the western area was lower than that in the eastern and southern area of the PRE on both days. The results indicate the potential for monitoring D_v^{50} on a large scale with Sentinel-2 MSI data.

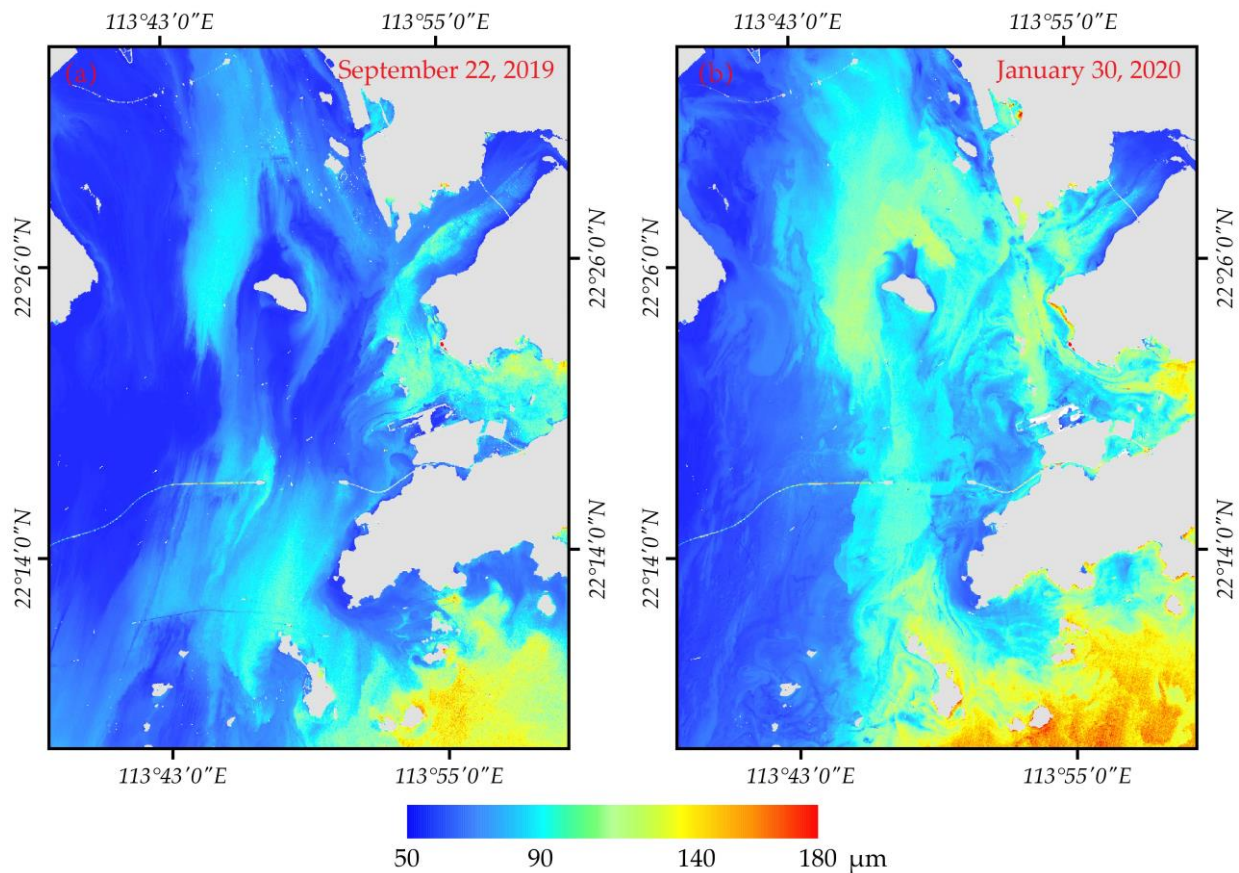


Figure 7. The D_v^{50} distribution retrieved by the proposed method on (a) 22 September 2019 and (b) 30 January 2020.

4. Discussion

4.1. Robustness of the D_v^{50} Model

Accurate estimation of $b_{bp}(\lambda)$ is of fundamental importance for accurate D_v^{50} retrieval. Some inversion models, such as Generalized IOP (GIOP) [47], the Garver–Seigel–Maritorena (GSM) algorithm [48], and the QAA [36], provide fairly accurate estimations of $b_{bp}(\lambda)$ for the open ocean, but they are less accurate in highly turbid or eutrophic coastal water [15]. We adopted 705 nm as the reference band in the QAA method, and thus the contribution of the absorption of CDOM and suspended particles to the total absorption in the reference band could be neglected. Consequently, the total absorption could be represented by pure water. In fact, the total absorption sometimes cannot be represented by pure water in the NIR band, especially for water with a high concentration of TSM [34]. In that case, the band in which water absorption is more obvious should be considered, such as the bands in the mid-infrared region [38].

It is known from previous studies that the backscattering ratio $b_{bp}^{\sim}(\lambda)$ is impacted by the bulk refractive index and the relative proportion between small- and large-sized particles, and theoretically, a higher proportion of small-sized particles indicates a higher $b_{bp}^{\sim}(\lambda)$ value [29,42,49]. Thus, the $b_{bp}^{\sim}(\lambda)$ value is not always constant between different waters. McKee and Cunningham (2006) [50] found that $b_{bp}^{\sim}(\lambda)$ varied over an order of magnitude from 0.005 to 0.050 in the Irish Sea and its coastal area, and Petzold (2007) [51] found that $b_{bp}^{\sim}(\lambda)$ was 0.019 for turbid waters in a San Diego harbor and 0.013 for the coastal waters. That aside, Loisel et al. (2007) [52] found that the value of $b_{bp}^{\sim}(\lambda)$ was

highly related to the refractive index of particles and that particle populations dominated by phytoplankton or inorganic particles were the trigger for higher or lower values of $b_{bp}(\lambda)$, respectively. In the present study, $b_{bp}(\lambda)$ was regarded as a constant value, and the fitted $b_{bp}(\lambda)$ of 0.0202 was in line with previous studies performed in different coastal and oceanic waters. However, the value of $b_{bp}(\lambda)$ should be discussed accordingly over the long term and with a large number of observations to ensure the accuracy of the D_v^{50} model.

In general, $b_p(\lambda)$ and $b_{bp}(\lambda)$ are driven by the particle concentration to the first order, whereas the particle size, refractive index, internal structure, and shape are driven to the second order [11,52]. In light of this, the relationships between the particle volume concentration $V(D)$ against $b_p(532)$, $b_{bp}(532)$, and $c_p(670)$ as measured by the LISST were observed (Figure 8). Consequently, the $b_p(532)$ and $V(D)$ in the particle size range between 3.7 and 85.2 μm showed a great correlation, and similar results were also found for $b_{bp}(532)$ and $c_p(670)$. However, there turned out to be a poor correlation when focusing on smaller and larger particles. These results might be explained by small particles that were not well-proportioned (Figure 8b) and particles that deviated from the “Junge distribution” model [53] when the particle size was smaller than 3.7 μm , while larger particles contributed less to the scattering because larger particles generally corresponded to phytoplankton that had a low refractive index, and this finding is in agreement with a previous study [52]. On account of these uncertainties, the estimation of $V_{tot}(D)$ (in a size range of 2.05–297 μm) from $b_p(\lambda)$ or $b_{bp}(\lambda)$ did not perform excellently. In addition, the relatively good correlation between D_v^{50} and $b_p^*(\lambda)$ with a negative exponential model supports the use of remote sensing to describe the PSD in the coastal water of the PRE.

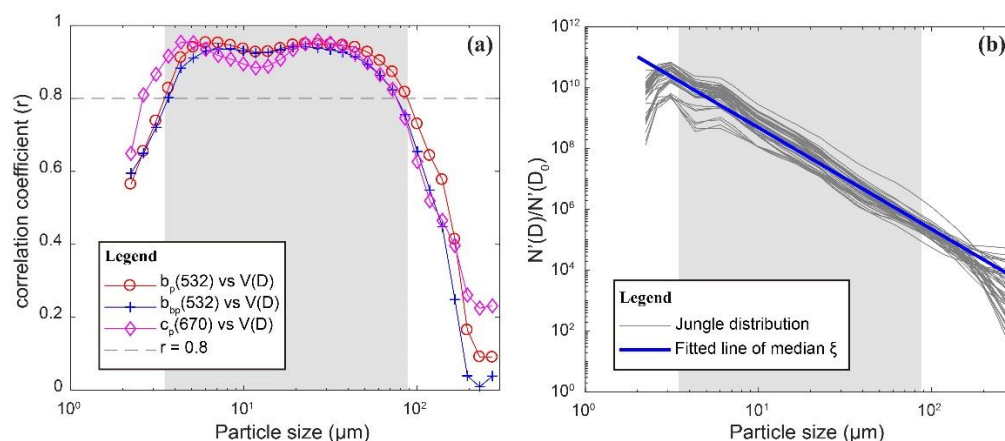


Figure 8. (a) Correlations between $V(D)$ and $b_p(532)$, $b_{bp}(532)$, and $c_p(670)$ in all size ranges (the gray region shows the particle size range within the correlation coefficient $r > 0.8$ for $b_p(532)$). (b) The “Junge distribution” for the particle number concentration (the blue line represents the fitted line of the median PSD slope ($\xi = 3.55$) of all the data).

4.2. Applicability to Sentinel-2 MSI Data

Sentinel-2 MSI was designed initially for land feature monitoring, and a higher signal-to-noise ratio is required for information extraction from water. However, some studies found that it performed well in inland and coastal water areas for water components or optical properties research [15,35]. The D_v^{50} distribution obtained from Sentinel-2 MSI showed that the water areas surrounding islands are full of small-sized particles. This finding is in agreement with previous studies that proposed that sediment resuspension occurs under high winds or tides in coastal water with a shallow bathymetry [54] and that small-sized particles are usually dominated by inorganic particles [1,11]. In general, large particles are dominated by phytoplankton or algae [55]. Therefore, D_v^{50} may be used as an indicator for the variation of phytoplankton and inorganic particle distribution.

5. Conclusions

A four-step method was presented for suspended particle size estimation in the coastal water areas in the PRE through establishing the relationship between D_v^{50} and the IOPs, which could be retrieved from the $R_{rs}(\lambda)$ of the water surface. As a consequence, the four-step method performed well for D_v^{50} estimation. However, there are still some limitations that should be considered in future work, such as the value of $b_{bp} \sim (\lambda)$ should be discussed according to long-term observations, and the $V_{tot}(D)$ calculated by $b_p(\lambda)$ is size-dependent. Nevertheless, we found that the in situ hyperspectral data resampled by the Sentinel 2 MSI channels had great potential for monitoring D_v^{50} in the coastal area. The above results provide the possibility to monitor the suspended particle size of coastal complex waters using a remote sensing method.

Author Contributions: Conceptualization, Z.W.; data curation, Z.W. and S.H.; formal analysis, Z.W., S.H., Q.L. and G.W.; funding acquisition, Z.W. and S.H.; methodology, Z.W.; writing—original draft, Z.W.; writing—review and editing, S.H., Q.L., H.L., X.L. and G.W. All authors have read and agreed to the published version of the manuscript.

Funding: This research was funded by the Guangdong Basic and Applied Basic Research Foundation (grant no. 2019A1515111181), Foundation of China grants (grant no. 41890852), and the Guangdong MEPP Fund (grant no. GDOE(2019)A48).

Institutional Review Board Statement: Not applicable.

Informed Consent Statement: Not applicable.

Acknowledgments: We sincerely thank the ESA's Copernicus Open Access Hub for distributing the Sentinel-2 data and for providing the SNAP software for free. We also thank the contributions of Chenchen Zhang and Guanning Wei to the field investigation. Our deepest gratitude goes to the anonymous reviewers for their careful work and thoughtful suggestions that have helped improve this paper substantially.

Conflicts of Interest: The authors declare no conflict of interest.

Abbreviations

Variables or Abbreviations	Description
a	Absorption coefficient
a_w	Absorption coefficient of pure water
b_b	Backscattering coefficient
b_{bp}	Backscattering coefficient of the particle
$b_{bp} \sim$	Backscattering ratio of the particle
b_{bw}	Backscattering of pure water
b_{bp}^*	Volume-specific backscattering coefficient of the particle
b_p	Scattering coefficient of the particle
b_p^*	Volume-specific scattering coefficient of the particle
c	Attenuation coefficient
CDOM	Colored dissolved organic matter
Chl- <i>a</i>	Chlorophyll- <i>a</i>
D_A	Mean diameter weighted by the area
D_v^{50}	Median particle diameter
IOPs	Inherent optical properties
L_w	Radiance of the water's surface
L_p	Radiance of the reference panel
L_{sky}	Radiance of the sky
$N(D)$	Particle number concentration
PRE	Pearl River estuary
PSD	Particle size distribution
Q_{be}	Scattering efficiency
R_{rs}	Remote sensing reflectance just above the water's surface

Variables or Abbreviations	Description
r_{rs}	Remote sensing reflectance just beneath the water's surface
SRF	Spectral response function
TSM	Total suspended mater
u	Ratio of backscattering and summation of absorption and backscattering
$V(D)$	Particle volume concentration
$V_{tot}(D)$	Total volume concentration of the particle
Y	Slope of the backscattering coefficient
ξ	PSD slope
ρ	Air–water reflectance
ρ_a	Apparent density
ρ_p	Diffuse reflectance of the reference panel

References

1. Xi, H.; Larouche, P.; Tang, S.; Michel, C. Characterization and variability of particle size distributions in Hudson Bay, Canada. *J. Geophys. Res. Ocean.* **2014**, *119*, 3392–3406. [[CrossRef](#)]
2. Qiu, Z.; Sun, D.; Hu, C.; Wang, S.; Zheng, L.; Huan, Y.; Peng, T. Variability of particle size distributions in the Bohai Sea and the Yellow Sea. *Remote Sens.* **2016**, *8*, 949. [[CrossRef](#)]
3. Bowers, D.G.; Binding, C.E.; Ellis, K.M. Satellite remote sensing of the geographical distribution of suspended particle size in an energetic shelf sea. *Estuar. Coast. Shelf Sci.* **2007**, *73*, 457–466. [[CrossRef](#)]
4. Van der Lee, E.M.; Bowers, D.G.; Kyte, E. Remote sensing of temporal and spatial patterns of suspended particle size in the Irish Sea in relation to the Kolmogorov microscale. *Cont. Shelf Res.* **2009**, *29*, 1213–1225. [[CrossRef](#)]
5. Sun, D.; Qiu, Z.; Hu, C.; Wang, S.; Wang, L.; Zheng, L.; Peng, T.; He, Y. A hybrid method to estimate suspended particle sizes from satellite measurements over Bohai Sea and Yellow Sea. *J. Geophys. Res. Ocean.* **2016**, *121*, 6742–6761. [[CrossRef](#)]
6. Bader, H. The hyperbolic distribution of particle sizes. *J. Geophys. Res.* **1970**, *75*, 2822–2830. [[CrossRef](#)]
7. Reynolds, R.A.; Stramski, D.; Wright, V.M.; Wo'zniak, S.B. Measurements and characterization of particle size distributions in coastal waters. *J. Geophys. Res.* **2010**, *115*, C08024. [[CrossRef](#)]
8. Rodriguez-Trujillo, R.; Mills, C.A.; Samitier, J.; Gomila, G. Low cost micro-Coulter counter with hydrodynamic focusing. *Microfluid. Nanofluid.* **2007**, *3*, 171–176. [[CrossRef](#)]
9. Neukermans, G.; Loisel, H.; Mériaux, X.; Astoreca, R.; McKee, D. In situ variability of mass-specific beam attenuation and backscattering of marine particles with respect to particle size, density, and composition. *Limnol. Oceanogr.* **2012**, *57*, 124–144. [[CrossRef](#)]
10. Kostadinov, T.S.; Siegel, D.A.; Maritorea, S. Retrieval of the particle size distribution from satellite ocean color observations. *J. Geophys. Res. Ocean.* **2009**, *114*, C09015. [[CrossRef](#)]
11. Wang, S.; Qiu, Z.; Sun, D.; Shen, X.; Zhang, H. Light beam attenuation and backscattering properties of particles in the Bohai Sea and Yellow Sea with relation to biogeochemical properties. *J. Geophys. Res. Ocean.* **2016**, *121*, 3955–3969. [[CrossRef](#)]
12. Mie, G. Beiträge zur Optik trüber Medien, speziell kolloidaler Metallösungen. *Ann. Phys.* **1908**, *330*, 377–445. [[CrossRef](#)]
13. Qing, S.; Zhang, J.; Cui, T.; Bao, Y. Remote sensing retrieval of inorganic suspended particle size in the Bohai Sea. *Cont. Shelf Res.* **2014**, *73*, 64–71. [[CrossRef](#)]
14. Li, P.; Ke, Y.; Bai, J.; Zhang, S.; Chen, M.; Zhou, D. Spatiotemporal dynamics of suspended particulate matter in the Yellow River Estuary, China during the past two decades based on time-series Landsat and Sentinel-2 data. *Mar. Pollut. Bull.* **2019**, *149*, 110518. [[CrossRef](#)] [[PubMed](#)]
15. Balasubramanian, S.V.; Pahlevan, N.; Smith, B.; Binding, C.; Schalles, J.; Loisel, H.; Gurlin, D.; Greb, S.; Alikas, K.; Randla, M.; et al. Robust algorithm for estimating total suspended solids (TSS) in inland and nearshore coastal waters. *Remote Sens. Environ.* **2020**, *246*, 111768. [[CrossRef](#)]
16. Molkov, A.A.; Fedorov, S.V.; Pelevin, V.V.; Korchemkina, E.N. Regional models for high-resolution retrieval of chlorophyll a and TSM concentrations in the Gorky Reservoir by Sentinel-2 imagery. *Remote Sens.* **2019**, *11*, 1215. [[CrossRef](#)]
17. Zhan, W.; Wu, J.; Wei, X.; Tang, S.; Zhan, H. Spatio-temporal variation of the suspended sediment concentration in the Pearl River Estuary observed by MODIS during 2003–2015. *Cont. Shelf Res.* **2019**, *172*, 22–32. [[CrossRef](#)]
18. Yin, K.; Lin, Z.; Ke, Z. Temporal and spatial distribution of dissolved oxygen in the Pearl River Estuary and adjacent coastal waters. *Cont. Shelf Res.* **2004**, *24*, 1935–1948. [[CrossRef](#)]
19. Buonassissi, C.J.; Dierssen, H.M. A regional comparison of particle size distributions and the power law approximation in oceanic and estuarine surface waters. *J. Geophys. Res. Ocean.* **2010**, *115*, C10028. [[CrossRef](#)]
20. Huang, J.; Chen, X.; Jiang, T.; Yang, F.; Chen, L.; Yan, L. Variability of particle size distribution with respect to inherent optical properties in Poyang Lake, China. *Appl. Opt.* **2016**, *55*, 5821–5829. [[CrossRef](#)]
21. Lei, S.; Wu, D.; Li, Y.; Wang, Q.; Huang, C.; Liu, G.; Zheng, Z.; Du, C.; Mu, M.; Xu, J.; et al. Remote sensing monitoring of the suspended particle size in Hongze Lake based on GF-1 data. *Int. J. Remote Sens.* **2019**, *40*, 3179–3203. [[CrossRef](#)]
22. Sequoia Scientific. *LISST-200X User's Manual (Version 1.3B)*; Sequoia Scientific, Inc.: Bellevue, WA, USA, 2018.

23. Jiang, D.; Zhang, H.; Zou, T.; Li, Y.; Tang, C.; Li, R. Suspended particle size retrieval based on geostationary ocean color imager (GOCI) in the Bohai Sea. *J. Coast. Res.* **2016**, *74*, 117–125. [[CrossRef](#)]
24. Slade, W.H.; Boss, E. Spectral attenuation and backscattering as indicators of average particle size. *Appl. Opt.* **2015**, *54*, 7264–7277. [[CrossRef](#)]
25. Agrawal, Y.C.; Pottsmith, H.C. Instruments for particle size and settling velocity observations in sediment transport. *Mar. Geol.* **2000**, *168*, 89–114. [[CrossRef](#)]
26. Mueller, J.L.; Brown, S.W.; Clark, D.K.; Johnson, B.C.; Yoon, H.; Lykke, K.R.; Flora, S.J.; Feinholz, M.E.; Souaidia, N.; Pietras, C. *Ocean Optics Protocols for Satellite Ocean Color Sensor Validation, Revision 5, Volume VI: Special Topics in Ocean Optics Protocols, Part 2*; Muller, J.L., Fargion, G.S., McClain, C.R., Eds.; NASA Goddard Space Flight Space Center: Greenbelt, MD, USA, 2004; pp. 1–63.
27. Wang, Z.; Kawamura, K.; Sakuno, Y.; Fan, X.; Gong, Z.; Lim, J. Retrieval of Chlorophyll-*a* and Total Suspended Solids Using Iterative Stepwise Elimination Partial Least Squares (ISE-PLS) Regression Based on Field Hyperspectral Measurements in Irrigation Ponds in Higashihiroshima, Japan. *Remote Sens.* **2017**, *9*, 264. [[CrossRef](#)]
28. Mobley, C.D. Estimation of the remote-sensing reflectance from above-surface measurements. *Appl. Opt.* **1999**, *38*, 7442–7455. [[CrossRef](#)] [[PubMed](#)]
29. Lin, J.; Cao, W.; Wang, G.; Zhou, W.; Sun, Z.; Zhao, W. Inversion of bio-optical properties in the coastal upwelling waters of the northern South China Sea. *Cont. Shelf Res.* **2014**, *85*, 73–84. [[CrossRef](#)]
30. WET Labs. *AC Meter Protocol Document (Revision Q)*; WET Labs, Inc.: Philomath, OR, USA, 2011.
31. Sullivan, J.M.; Twardowski, M.S.; Zaneveld, J.R.V.; Moore, C.M.; Barnard, A.H.; Donaghay, P.L.; Rhoades, B. Hyperspectral temperature and salt dependencies of absorption by water and heavy water in the 400–750 nm spectral range. *Appl. Opt.* **2006**, *45*, 5294–5309. [[CrossRef](#)]
32. WET Labs. *Scattering Meter ECO BB9 User's Guide (Revision L)*; WET Labs, Inc.: Philomath, OR, USA, 2013.
33. Brockmann, C.; Doerffer, R.; Peters, M.; Kerstin, S.; Embacher, S.; Ruescas, A. Evolution of the C2RCC neural network for Sentinel 2 and 3 for the retrieval of ocean colour products in normal and extreme optically complex waters. In Proceedings of the ESA Living Planet, Prague, Czech Republic, 9–13 May 2016.
34. Pereira-Sandoval, M.; Ruescas, A.; Urrego, P.; Ruiz-Verdú, A.; Delegido, J.; Tenjo, C.; Soria-Perpinyà, X.; Vicente, E.; Soria, J.; Moreno, J. Evaluation of atmospheric correction algorithms over Spanish inland waters for sentinel-2 multi spectral imagery data. *Remote Sens.* **2019**, *11*, 1469. [[CrossRef](#)]
35. Warren, M.A.; Simis, S.G.; Martinez-Vicente, V.; Poser, K.; Bresciani, M.; Alikas, K.; Spyarakos, E.; Giardino, C.; Ansper, A. Assessment of atmospheric correction algorithms for the Sentinel-2A MultiSpectral Imager over coastal and inland waters. *Remote Sens. Environ.* **2019**, *225*, 267–289. [[CrossRef](#)]
36. Lee, Z.; Carder, K.L.; Arnone, R.A. Deriving inherent optical properties from water color: A multiband quasi-analytical algorithm for optically deep waters. *Appl. Opt.* **2002**, *41*, 5755–5772. [[CrossRef](#)] [[PubMed](#)]
37. Lee, Z.; Bertrand, L.; Jeremy, W.; Robert, A. An Update of the Quasi-Analytical Algorithm (QAA_v5). Technical Report, International Ocean Colour Coordinating Group (IOCCG). 2009. Available online: <http://www.ioccg.org/groups/software.html> (accessed on 2 December 2021).
38. Le, C.F.; Li, Y.M.; Zha, Y.; Sun, D.; Yin, B. Validation of a quasi-analytical algorithm for highly turbid eutrophic water of Meiliang Bay in Taihu Lake, China. *IEEE Trans. Geosci. Remote Sens.* **2009**, *47*, 2492–2500.
39. Li, S.; Song, K.; Mu, G.; Zhao, Y.; Ma, J.; Ren, J. Evaluation of the Quasi-Analytical Algorithm (QAA) for estimating total absorption coefficient of turbid inland Waters in Northeast China. *IEEE J. Sel. Top. Appl. Earth Obs. Remote Sens.* **2016**, *9*, 4022–4036. [[CrossRef](#)]
40. Buiteveld, H.; Hakvoort, J.H.M.; Donze, M. Optical properties of pure water. In Proceedings of the Ocean Optics XII, Bergen, Norway, 13–15 June 1994; 2258, pp. 174–183.
41. Boss, E.; Twardowski, M.S.; Herring, S. Shape of the particulate beam attenuation spectrum and its inversion to obtain the shape of the particulate size distribution. *Appl. Opt.* **2001**, *40*, 4885–4893. [[CrossRef](#)]
42. Twardowski, M.S.; Boss, E.; Macdonald, J.B.; Pegau, W.S.; Barnard, A.H.; Zaneveld, J.R.V. A model for estimating bulk refractive index from the optical backscattering ratio and the implications for understanding particle composition in case I and case II waters. *J. Geophys. Res. Ocean.* **2001**, *106*, 14129–14142. [[CrossRef](#)]
43. Sun, D.; Su, X.; Wang, S.; Qiu, Z.; Ling, Z.; Mao, Z.; He, Y. Variability of particulate backscattering ratio and its relations to particle intrinsic features in the Bohai Sea, Yellow Sea, and East China Sea. *Opt. Express* **2019**, *27*, 3074–3090. [[CrossRef](#)]
44. Whitmire, A.L.; Boss, E.; Cowles, T.J.; Pegau, W.S. Spectral variability of the particulate backscattering ratio. *Opt. Express* **2007**, *15*, 7019–7031. [[CrossRef](#)]
45. Martinez-Vicente, V.; Land, P.E.; Tilstone, G.H.; Widdicombe, C.; Fishwick, J.R. Particulate scattering and backscattering related to water constituents and seasonal changes in the Western English Channel. *J. Plankton Res.* **2010**, *32*, 603–619. [[CrossRef](#)]
46. Woźniak, S.B.; Stramski, D.; Stramska, M.; Reynolds, R.A.; Wright, V.M.; Miksic, E.Y.; Cichocka, M.; Cieplak, A.M. Optical variability of seawater in relation to particle concentration, composition, and size distribution in the nearshore marine environment at Imperial Beach, California. *J. Geophys. Res. Ocean.* **2010**, *115*, C08027. [[CrossRef](#)]
47. Werdell, P.J.; Franz, B.A.; Bailey, S.W.; Feldman, G.C.; Boss, E.; Brando, V.E.; Dowell, M.; Hirata, T.; Lavender, S.J.; Lee, Z.; et al. Generalized ocean color inversion model for retrieving marine inherent optical properties. *Appl. Opt.* **2013**, *52*, 2019–2037. [[CrossRef](#)] [[PubMed](#)]

48. Maritorena, S.; Siegel, D.A.; Peterson, A.R. Optimization of a semianalytical ocean color model for global-scale applications. *Appl. Opt.* **2002**, *41*, 2705–2714. [[CrossRef](#)] [[PubMed](#)]
49. Ulloa, O.; Sathyendranath, S.; Platt, T. Effect of the particle-size distribution on the backscattering ratio in seawater. *Appl. Opt.* **1994**, *33*, 7070–7077. [[CrossRef](#)]
50. McKee, D.; Cunningham, A. Identification and characterisation of two optical water types in the Irish Sea from in situ inherent optical properties and seawater constituents. *Estuar. Coast. Shelf Sci.* **2006**, *68*, 305–316. [[CrossRef](#)]
51. Petzold, T.J. *Volume Scattering Functions for Selected Ocean Waters*; Scripps Institution of Oceanography: La Jolla, CA, USA, 1972.
52. Loisel, H.; Mériaux, X.; Berthon, J.F.; Poteau, A. Investigation of the optical backscattering to scattering ratio of marine particles in relation to their biogeochemical composition in the eastern English Channel and southern North Sea. *Limnol. Oceanogr.* **2007**, *52*, 739–752. [[CrossRef](#)]
53. Junge, C.E. *Air Chemistry and Radioactivity*; Academic Press Inc.: New York, NY, USA, 1963; p. 382.
54. Cui, T.W.; Zhang, J.; Ma, Y.; Zhao, W.J.; Sun, L. The study on the distribution of suspended particulate matter in the Bohai Sea by remote sensing. *Acta Oceanol. Sin.* **2009**, *31*, 10–18.
55. Koestner, D.; Stramski, D.; Reynolds, R.A. Assessing the effects of particle size and composition on light scattering through measurements of size-fractionated seawater samples. *Limnol. Oceanogr.* **2020**, *65*, 173–190. [[CrossRef](#)]